



Fractal breakage of porous carbonate sand particles: Microstructures and mechanisms

H.Y. Li ^a, H.W. Chai ^b, X.H. Xiao ^c, J.Y. Huang ^{a,b,*}, S.N. Luo ^{a,b,*}

^a Key Laboratory of Advanced Technologies of Materials, Ministry of Education, Southwest Jiaotong University, Chengdu, Sichuan 610031, PR China

^b The Peac Institute of Multiscale Sciences, Chengdu, Sichuan 610031, PR China

^c Advanced Photon Source, Argonne National Laboratory, Argonne, IL 60439, USA

ARTICLE INFO

Article history:

Received 2 May 2019

Received in revised form 2 January 2020

Accepted 5 January 2020

Available online 7 January 2020

Keywords:

Carbonate sands

In situ tomography

Intra-granular pores

Fractal breakage

Cleavage

ABSTRACT

In situ, three-dimensional (3D) characterizations of particle breakage in porous carbonate sands are presented, for the first time, with synchrotron-based micro computed tomography. Evolution of grain-scale characteristics are identified and quantified via elaborate image processing and topology analyses. The sequential 3D images reveal distinctly different fracture mechanisms for carbonate sands from silica sands. The angular shape of carbonate sand particles facilitates bending fracture, and particles with a lower sphericity and a higher porosity are more prone to break. 3D crack networks extracted from fractured particles imply considerable cleavage along initial pores. The fractal dimension of crack networks increases with external loading due to crack branching via cleavage. The resultant fragment size distribution also appears fractal and the fractal feature is valid down to the breakage limit of calcium carbonate. Crack propagation along the initial pores reduces the energy barrier for particle breakage and thus fracture strength of particles.

© 2020 Elsevier B.V. All rights reserved.

1. Introduction

Carbonate sands are widely distributed in coral reefs and seashores across such regions as South China Sea, Red Sea, West Australia Continental Platform, and Bass Strait [1]. As the key construction material in islands, they are commonly used for road embankments and airport runways in offshore geotechnical engineering [1,2], and are also a promising source for coral concrete [3]. However, the fragility and porousness of carbonate sand pose great threats to offshore engineering. In 1968, crushed carbonate sands led to an unexpected free fall of a pile during pile driving for the Lavan petroleum platform in offshore Iran [2]. In addition, carbonate sediments were observed to liquefy and spread due to seismic or wave loading [4,5], causing catastrophic damage to offshore structures. Therefore, understanding the geological and mechanical properties of carbonate sands, as well as the related microstructures and fracture mechanisms, is critical for optimal structural design in such engineering applications.

Carbonate sands are composed of the remains of marine organisms such as shells and detrital corals, which are generally thin-walled bodies with abundant internal voids and highly angular shapes [2,6]. The complex microstructure of carbonate soils hinders a comprehensive understanding of their mechanical response, and they have been classified as

'problematic soils' in geotechnical design [6]. Compared to more commonly studied silica sands [7–9], carbonate sands are rich in calcium carbonate, which owns much lower hardness than quartz. Moreover, the high intra-granular voids and irregular grain shapes render them fragile to mechanical loads [10–12]. Despite the recognition of strong microstructural dependence of the engineering properties, previous knowledge on the structure–property relationship of these sands was essentially qualitative and based on two-dimensional (2D) image analysis of thin sections [13] or particle projections [14]. With the increase of offshore activities in tropical regions where carbonate sands dominate, a more accurate description of their mechanical behavior along with the evolution of their 3D microstructures is in urgent need, but remains an experimental challenge [6].

Apart from sand/soil breakage in geotechnical engineering, particle breakage is commonly encountered in a number of applications, including mining [15], pharmaceutical/food industry [16] and powder technology [17–19]. Mechanical loading leads to disaggregation and breakage of agglomerates or particles, and thus alters the gradation of granular materials, which affects their mechanical and hydraulic performances. Particle breakage of carbonate sands under uniaxial compression has been extensively studied [10,20–22]. However, previous studies focused on statistical evolution of grain size distribution of granular samples. The breakage mechanisms at the grain scale and the effects of microstructures were basically inferred from postmortem analyses, e.g. via scanning electron microscopy (SEM) [22,23]. Discrete element modelling (DEM) is a useful tool in revealing mechanisms of

* Corresponding author at: The Peac Institute of Multiscale Sciences, Chengdu, Sichuan 610031, PR China

E-mail addresses: jyhuang@pims.ac.cn (J.Y. Huang), sluo@pims.ac.cn (S.N. Luo).

particle breakage [8,24,25]. The reliability of DEM depends highly on the input of initial granular configurations [25,26] and the set of breakage parameters and fracture modes of particles [27], which requires accurate experimental constraints on particle breakage including fragment morphology.

Understanding of the grain-scale properties of granular materials has been improved with advanced imaging techniques [28,29]. While optical imaging yields a surface measurement, X-rays are capable of mapping non-destructively the interior of optically opaque materials like soil and sand [6,30,31]. X-ray micro computed tomography (μ CT) is particularly useful to elucidate microstructural evolution with micro- or nano-meter resolution for better understanding of materials deformation dynamics [32,33]. CT has been widely applied to 3D microstructural analysis of granular materials [29,34–37]. For instance, Hurley et al. [28] developed a 3D X-ray diffraction (XRD) technique combining CT with XRD, and mapped directly the contact force field in crystalline quartz sand under elastic deformation. With μ CT, Wang and coworkers [26,38–40] conducted systematic work on 3D quantifications of grain morphology and fracture modes of silica sands. Given the technical challenge to image segmentation associated with complex shapes and high intra-granular pores, 3D characterization on carbonate sands is scarce. Among one of the few studies, Kong and Fonseca [6] performed a detailed morphological quantification of carbonate sands on grain shapes and sizes, while the pore morphology was left untouched.

Here we present for the first time in literature an in situ, 3D characterization for the particle breakage process of carbonate sands under mechanical loading. Using a miniature material test system (mini MTS) implemented with synchrotron-based μ CT [41], the intra-granular pore morphology and evolution of grain-scale characteristics are quantified. The sequential 3D images reveal clearly the structure–property relationship for carbonate sands. 3D crack networks extracted from fractured particles imply obvious cleavage along initial pores. The crack networks are fractal and the fractal dimension increases with external loading. The resultant fragment size distribution also appears fractal and the fractal feature can be extended down to the breakage limit of particles.

2. Materials and methodology

2.1. Materials

Carbonate sand in this study is sampled from an island in South China Sea. For simplicity, we focus on sand particles of ~ 1 mm sieved from the original sands after washing and drying.

2.2. Experimental setups and procedure

To elucidate the microstructural dependence of particle breakage for carbonate sands, in situ CT characterizations are carried out on sand particles. The experimental setup, as illustrated in Fig. 1, is implemented at the beamline 2BM, the Advanced Photon Source, Argonne National Laboratory. The upright mini MTS is designed for in situ CT under compression. The sample is sandwiched between two steel platens. An electrical motor drives a lead screw to lower the upper platen and compress the sample, while the lower platen is fixed. The load and platen displacement signals are recorded by sensors embedded in the platens and exported to a laptop. The upper loading and lower supporting parts are connected by a hollow polycarbonate (PC) tube. The PC window is of uniform material and yields little noise on the projection images. The hollow design above and below the PC tube facilitates quick and easy sample manipulations.

A simple loading geometry with 11 particles aligned sequentially in a column (Fig. 1 inset), is adopted. This geometry minimizes the complexity of random granular packing, and allows one to focus on the role of grain morphology (i.e. shape and porosity). Sand particles are placed in a 13 mm long polymethylmethacrylate (PMMA) tube, with

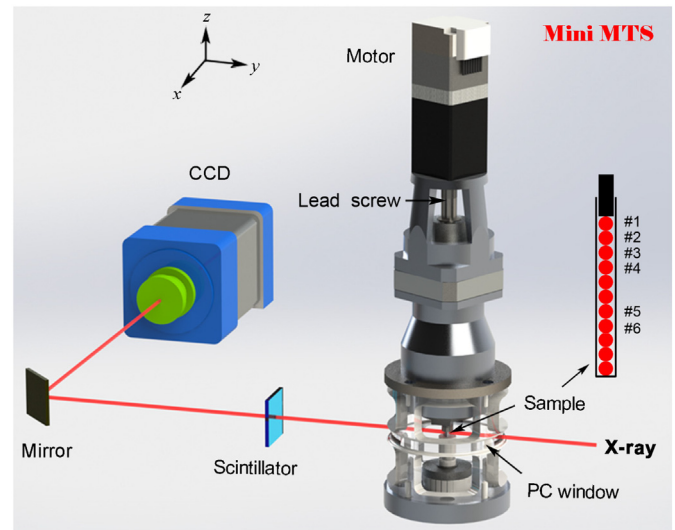


Fig. 1. Schematic diagram of the miniature MTS and in situ CT system.

an inner and outer diameter of 2 mm and 4 mm, respectively. A PMMA rod (diameter 1.9 mm, length 5 mm) is inserted to the PMMA tube and transmits loads to sand particles. The loading velocity is set as 0.005 mm s^{-1} . Sand particles of interest are scanned at different deformation levels to capture varying crushing states. When the preset platen displacement is achieved, the upper platen is fixed and CT-scan is carried out after the stress relaxes to a nearly stable state in about 30 s. A pause of loading for ~ 5 min is needed for a CT scan. X-rays transmitted through the sample form images on a $20 \mu\text{m}$ thick LuAG scintillator which are captured by a charge coupled device (CCD, 2560×2000 pixels). The projection data for each scan comprise 1500 radiographs in 0° – 180° , which are then reconstructed into volume data using an open-source program TomoPy [42]. The X-ray energy is set as 35 keV, the exposure time is 100 ms, and the sample-to-scintillator distance is 60 mm. The nominal resolution is $0.87 \mu\text{m}/\text{pixel}$.

2.3. Image processing

The reconstructed volume data are processed to identify and quantify the morphology of sand particles, initial pore networks, fragments and crack networks (Fig. 2). The accuracy of CT results depends on both the processing techniques, and the resolution and quality of gray-scale images. Compared to cone beam X-ray tomography [36,43,44], the synchrotron-based X-ray images are of much higher resolution ($0.87 \mu\text{m}$ per pixel) and quality. This facilitates image processing and the subsequent identification of topological structures. G. Kerckhofs et al. [43] proposed microscopy (e.g. SEM) as a “golden standard” to assess the accuracy of CT results by matching binarised CT slices with binarised microscopic images of the same section. However, it is impossible to conduct similar examinations for carbonate sand particles with complex shapes and intra-particle pores. Parametric studies are carried out on critical processing steps to select optimum parameters.

The morphology of sand particles and initial pore networks are identified in three steps (Fig. 2(a), s0–s6). Firstly, the solid phase (white) and the air phase (black) are segmented via thresholding segmentation (TS), and then are both eroded by 5 pixels (s1). Gray pixels refer to the undefined phase. After that, a marker-controlled watershed (MCW) algorithm [45] is applied to s0 to identify the surface profiles of particles (s2), using the “watershed tool” module embedded in Avizo. The threshold for TS shows little influence on the resultant image s2 in a wide range, because MCW detects the largest gray gradient and is not very sensitive to the marker (s1). The threshold is chosen as the mid-value of this range. Secondly, the classic watershed algorithm

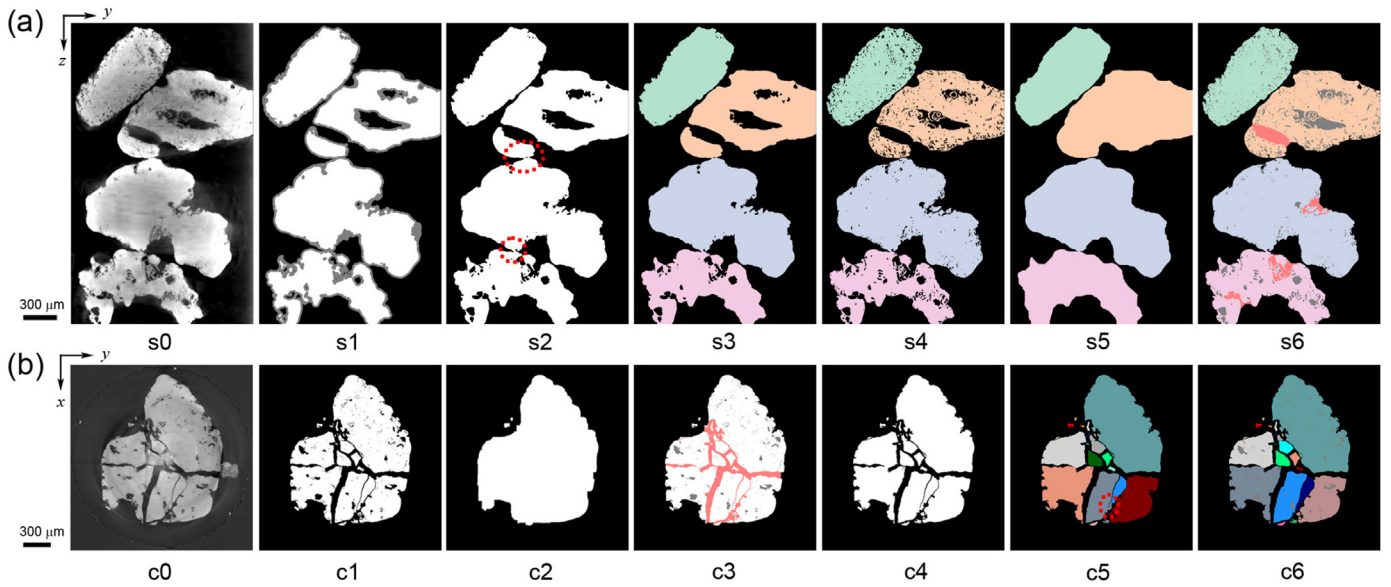


Fig. 2. (a) Image processing techniques and steps used to render sand particles and pore networks. s0: gray-scale yz slice; s1: thresholding segmentation and erosion; s2: marker-controlled watershed segmentation; s3: contact segmentation with classic watershed; s4: recover small enclosed pores with the top-hat method; s5: closing (dilation and erosion); s6: subtract s4 from s5, and identify enclosed pores (gray) and inner pores connected to the particle surface (red). (b) Image processing techniques and steps used to identify crack networks and fragments. c0: gray-scale xy slice; c1: separate the solid and air phase with steps s1–s4 in (a); c2: closing; c3: subtract c1 from c2, and identify crack networks; c4: fill pores; c5: classic watershed segmentation; c6: repair over-segmentation manually.

[46] is used to segment particle contacts. Contact segmentation is implemented well with classic watershed (s3) and not affected by intra-particle pores [6] in our case, mainly because small pores remain filled during this step and high resolution images result in a tiny contact area between particles [36]. A simple contact geometry (marked by dashed ellipses in s2) also facilitates contact segmentation. The third step (s4–s6) is to identify the intra-particle pore networks which consist of enclosed pores inside particles, and inner pores connected to the particle surface. Compared to surface concaves, the inner pores are more slender and penetrate deeper into particles. The relatively large enclosed pores can be extracted naturally from the air phase by combined TS and MCW segmentation. The remaining (small) enclosed pores, buried in the solid phase after TS, are recovered as follows. A top-hat transform [47] is applied to s0; the small enclosed pores can then be extracted via TS on the transformed image; finally, those pore voxels located in the solid phase are superimposed on s3, to obtain s4. The threshold for TS affects significantly the extraction of pores, and the optimum value is determined by visual comparison between the extracted pores and the gray-scale image. The inner pores, also dropped into the air phase after TS, are resumed in the following steps: (i) perform a closing operation (dilation and erosion) on s4; the closing parameters have little influence on the extraction of inner pores; (ii) subtract s4 from the obtained image s5 to extract the pore phase (including some surface concaves); (iii) pick out the enclosed pores (marked gray in s6) by a connectivity test between the pore phase and air phase, and then the inner pores (marked red in s6) by visual inspection. Therefore, the morphologies of particles (color code) and initial pore networks (gray and red) are identified with full details.

Sand particles fragment when the load exceeds a critical value. The fragments, cracks, and intra-fragment pores are segmented to quantify their 3D morphology (Fig. 2(b), c0–c6). First of all, the steps s1–s4 in Fig. 2(a) are repeated on the gray-scale volume image c0, and thus the solid phase and air phase are fully separated (c1). Then a closing operation is performed on c1. The pore and crack phases are extracted by subtracting c1 from the obtained image c2. Cracks are distinctly different from initial pores in morphology; for example, cracks are flat with rough surfaces while pores are mostly tubular with smooth surfaces. Therefore, the crack phase (marked red in c3) can be easily picked out via visual inspection. From a quantitative point of view, the surface roughness and

the morphological parameters (e.g., flatness/elongation index [38]) can be adopted to distinguish cracks from initial pores. The size limit for crack detection is resulted from the resolution of imaging, at around 5 μm . After that, pores in particles are filled (c4) and the classic watershed algorithm is used to segment fragments (c5). The segmentation parameters are chosen to guarantee that all fragments are segmented and to minimize over-segmentation. The fragment partitioning is visually inspected to repair over-segmented fragments (as marked by the dashed ellipse in c5). The intra-fragment pores are identified with the same process shown in Fig. 2(a), s4–s6. The morphology of cracks, fragments and intra-fragment pores is thus identified (c6).

2.4. Topology analyses

2.4.1. Gyration-tensor based shape parameters

A gyration tensor G is introduced to characterize the topology of particles [48,49],

$$G_{\alpha\beta} = \frac{1}{V_m} \sum_{i=1}^{V_m} (r_{\alpha i}^{(m)} - r_{\alpha}^{(b)}) (r_{\beta i}^{(m)} - r_{\beta}^{(b)}), \quad (1)$$

where $r_{\alpha i}^{(m)}$ ($r_{\beta i}^{(m)}$) and $r_{\alpha}^{(b)}$ ($r_{\beta}^{(b)}$) ($\alpha, \beta = x, y, z$) are coordinates of voxel i , and of the barycentre (b) of particle m , respectively. V_m is the volume of particle m (in terms of the number of voxels occupied). The eigenvalues of the gyration tensor are calculated as R_1, R_2 and R_3 ($R_1 > R_2 > R_3$). Then, a characteristic ellipsoid (Fig. 3(a)) can be constructed with three semi-axes oriented along the eigenvectors, and their lengths are $a = \sqrt{5R_1}$, $b = \sqrt{5R_2}$ and $c = \sqrt{5R_3}$ ($a > b > c$).

Then two aspect ratios, the flatness index (FI) and the elongation index (EI), are obtained as

$$\text{FI} = R_3/R_2; \quad \text{EI} = R_2/R_1 \quad (2)$$

The sphericity index S_1 can be defined with the eigenvalues as

$$S_1 = 1 - \frac{1}{2} \frac{\sum_{i,j}^3 (R_i - R_j)^2}{\left(\sum_i^3 R_i\right)^2}, \quad (3)$$

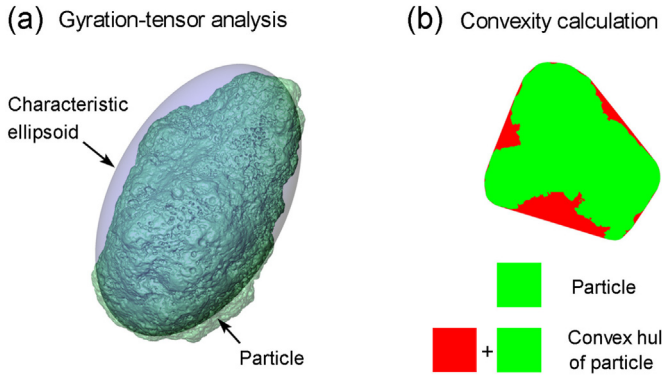


Fig. 3. Schematic diagrams for (a) gyration tensor analysis and (b) convexity calculation.

The classic sphericity index S_0 is defined as

$$S_0 = \sqrt[3]{36\pi V_m^2 / S_r} \quad (4)$$

where S_r is the real surface area of particle m .

The convexity C_x is defined as

$$C_x = V / V_{CH} \quad (5)$$

where V is particle volume and V_{CH} is the volume of the convex hull enclosing the particle [6]. A convex hull is defined as the minimum convex surface containing all voxels of the particle (Fig. 3(b)).

2.4.2. Box-counting method

The 3D box-counting method is adopted to derive the fractal dimension D of pore and crack networks. For a 3D fractal object, the estimation procedure contains three steps [50]. First, cubic box units with a reasonable size r is chosen and stacked side by side to encompass the whole fractal object. Then the minimal number of nonempty boxes $N(r)$ required to completely cover the whole fractal object is counted. After that, one decreases the box size r and repeats the same counting process. The $N(r) - r$ relation follows a power law, which defines the fractal dimension D as

$$N(r) = C_1 r^{-D} \quad (6)$$

3. Results

Initial CT characterizations are carried out on all 11 particles while 6 particles (marked in the inset of Fig. 1) are chosen for in situ CT characterization. Particles labeled #1–#4 are used to discuss qualitatively the effects of particle shape and porosity on particle breakage. Since particle breakage in these particles is too fast for tracking the evolution of 3D fracture patterns, another two particles labeled #5–#6 are used for a quantitative characterization of the fracture networks and fragment morphology, where particles break more progressively. The shape parameters of these six particles are calculated and summarized in Table 1.

3.1. Grain morphology and fractal pores

The 3D rendering of three representative particles and corresponding pore networks are illustrated in Fig. 4(a). The volume of intra-particle pores is used to calculate the porosity of particles. The porosity (2%–30%) and pore morphology (e.g., shape, size and distribution) differ markedly for different particles, probably due to the diverse biogenic origin of carbonate sand particles. Interestingly, coral-shaped pore networks are found in several particles. Such a pore network comprises many tubular pores and a central spheroidal pore filled with organic

Table 1

Shape parameters of the six particles selected for in situ CT characterizations. d : equivalent sphere diameter; S_0 : classic sphericity index; S_1 : gyration-tensor defined sphericity index; C_x : convexity; EI: elongation index; FI: flatness index; n : ratio of pore volume to the particle volume; D_p : fractal dimension of pores. See the Section 2.4 for the detailed definition of the shape parameters.

Particle number	d (mm)	S_0	S_1	C_x	EI	FI	n	D_p
#1	1.09	0.70	0.86	0.96	0.63	0.32	11.2%	2.44
#2	1.19	0.60	0.86	0.87	0.56	0.36	13.4%	2.47
#3	1.18	0.59	0.90	0.87	0.60	0.53	4.0%	2.24
#4	1.06	0.51	0.82	0.75	0.55	0.29	15.6%	2.41
#5	1.11	0.61	0.72	0.91	0.35	0.38	17.4%	2.44
#6	1.35	0.50	0.68	0.92	0.30	0.42	10.7%	2.45

matter, probably due to biogenic sedimentation. The 3D tubular pores are consistent with the high-density circular voids observed in SEM images [51]. The pore network shows a fractal feature, and the fractal dimension is estimated via the 3D box-counting method [50,52]. The fractal dimension increases with porosity of sand particles, and their

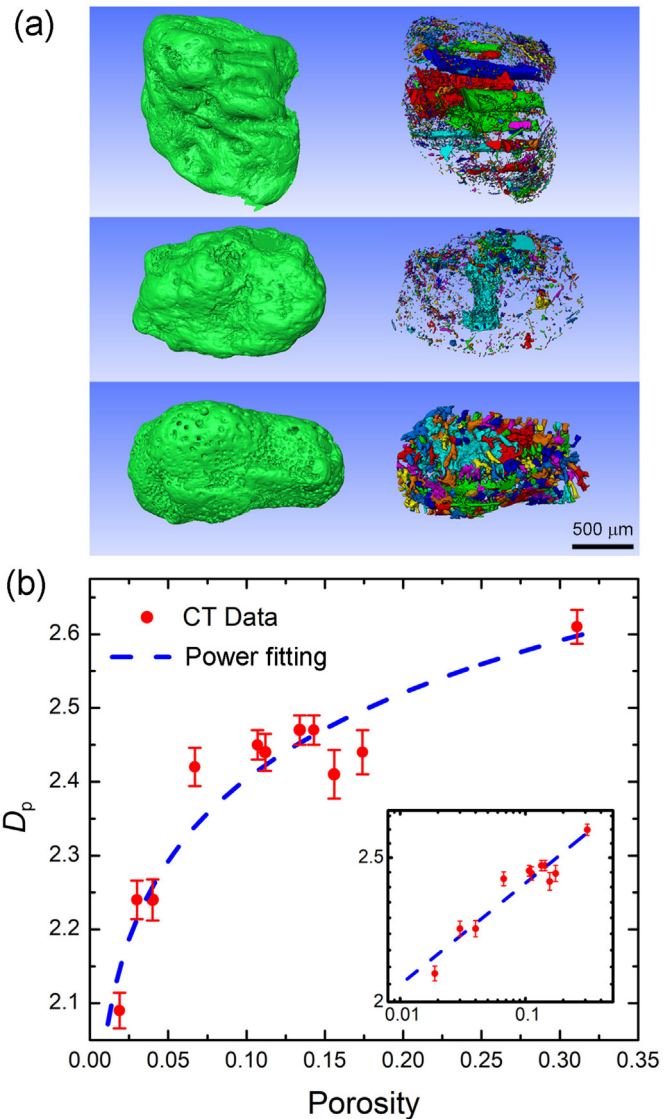


Fig. 4. (a) Representative 3D images of sand particles (left column) and intra-granular pores (right column) prior to compression. Colorcode in intra-granular pores represents the interconnectivity between different pores. (b) Fractal dimension D_p of pore networks as a function of grain porosity, along with a power-law fitting. Inset: the log-log plot.

relation follows a power law (Fig. 4(b)). The mean fractal dimension is ~ 2.4 .

The diverse pore morphology results in a scattered fracture strength distribution of carbonate sand particles. Single-particle compression tests are carried out on 40 spheroidal particles, and their fracture strengths σ_s are calculated. σ_s refers to the fracture strength associated with tensile splitting, and is characteristic of brittle spheroidal particles under uniaxial compression. It is calculated as [18,53]

$$\sigma_s = C \frac{F}{d^2}, \quad (7)$$

where F is taken as the maximum force right before a catastrophic drop in force on the compression curve, and d is the equivalent diameter of a particle projection along the compression axis. C depends on the contact radius and breakage mode of particles [18] and is taken as 1.0 here. The Weibull statistics [53] (Appendix) is adopted to derive the Weibull modulus m and characteristic strength σ_{s0} (Fig. 5), and the results are $m = 3.6 \pm 0.1$, $\sigma_{s0} = 26.4 \pm 1.1$ MPa. The Weibull modulus is slightly higher than those (1.88–2.56) reported for carbonate sand particles in previous literatures [11,54], probably because spheroidal particles are used in this work while particles with diverse shapes are used in literatures.

3.2. Microstructural dependence of particle breakage

The compression curve along with the 3D rendering and 2D slices of four sand particles (#1–#4) is presented in Fig. 6. The load–displacement curve (Fig. 6(a)) exhibits several stress plateaus, due to particle breakage or rearrangement as illustrated in 3D images (Fig. 6(b)). The particles are of similar sizes (Table 1), and have similar neighboring contacts (4–6). However, they are broken at different stress levels with different modes. Particle #4 breaks first by bending fracture (marked by arrows at frame f1, Fig. 6(c)), followed by particle #2 with tensile splitting (frame f2, Fig. 6(d)), and then particle #1 with mainly contact attrition (frame f4, Fig. 6(d)). Particle #3 exhibits little damage and fracture during loading.

The shape parameters and initial porosity of four particles vary significantly. Particle #4 has the smallest convexity and thus the most angular shape. The bumps and hollows on its surface form a three-point bending geometry with neighboring particles. Particle #4 is subjected

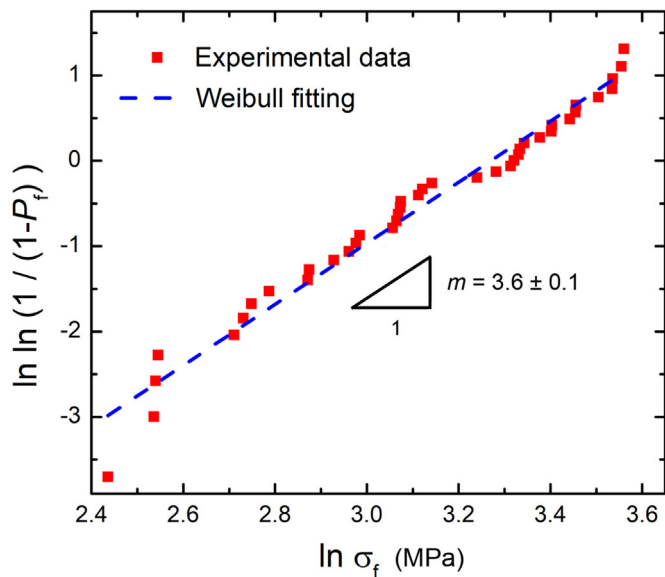


Fig. 5. Probability of failure P_f versus fracture strength σ_f of sand particles, along with the Weibull analysis (dashed line). The Weibull modulus $m = 3.6 \pm 0.1$.

to bending fracture at the lowest bulk load level. The tensile stress can be calculated according to the classic beam theory as $\sigma_b = 3FL/(2wh^2) = 21.7$ MPa, where F is the bulk force, L is the spanning distance between two support points, and b and h are the equivalent width and thickness of the particle, respectively. σ_b is comparable to the tensile strength of solid calcium carbonate. However, if we do not have access to the breakage mode of particles and still assume tensile splitting, the

fracture strength of particle #4 will be calculated as $\sigma_s = F/(Lwh)^2 = 6.6$ MPa, which significantly underestimates the real fracture strength. In other words, the angular shape of particle #4 results in tensile stress concentration in it and thus its early failure. In addition, particle #4 has the highest porosity which also degrades its strength and leads to multiple fragmentation in the subsequent loading process. The shape parameters of particles #1–#3 are similar. The porosity of particle #2 is higher than that of particle #1. Hence it has a lower fracture strength and breaks before particle #1. Particle #3 has the lowest porosity and the most spherical shape, which results in a higher particle strength but a lower tensile stress in the particle compared to the other particles, and delays its breakage. Therefore, the microstructures including the particle and pore morphologies determine the breakage strength and modes of particles at the microscopic scale, and consequently influence the macroscopic properties (stress plateaus and drops) of carbonate sands. Therefore, 3D grain morphology should be taken into account in numerical modelling of carbonate sands.

3.3. Crack morphology and fractal breakage

Particles #5 and #6 are selected to examine the morphological evolution of cracks and fragments (Fig. 7(a)). Tensile splitting occurs in both particles (marked by arrows) at frame f2 before which the particles remain intact. Secondary fracture occurs in the fragments of particle #6 at frame f3. Evolution of the crack networks in particles #5 and #6 at different instants are presented in Fig. 7(b) and (c), respectively. A straight main crack is observed at frame f2 in both particles, and then crack branching (marked by arrows) develops around the main crack at frames f3 and f4 as particle breakage progresses. At frame f2, the volume of cracks of particle #5 is higher than that of particle #6, indicating that particle breakage occurs earlier in particle #5. This is consistent with the higher porosity and thus lower fracture strength of particle #5. The crack network exhibits a fractal configuration, and the fractal dimension D_c is also calculated via the box-counting method (Fig. 8). D_c increases considerably with external loading and the breakage extent of particles, and approaches that of the initial pore network (~ 2.4).

To discuss the effect of initial pores on the crack path, xy slices of particle #5 at different instants (f1–f3) are presented in Fig. 9(a). At frame f2, a main crack (marked by the arrow) initiates and shows signals of branching. The branching cracks (marked by arrows at frame f3) grow and propagate along the pore-rich paths (illustrated by dashed arrows at frame f1). This effect can be quantified by counting the number of such pores connected by the crack network [55]. A crack “porosity” ϕ_c can be defined as the number of pore voxels in the crack network, divided by the number of crack voxels.

$$\phi_c = \frac{V_{p,c}}{V_c}. \quad (8)$$

Here V_c is the volume of cracks consisting of two parts, i.e. the cracks generated in the solid phase V_c^* and in the initial pore phase $V_{p,c}$. To calculate $V_{p,c}$, the volume of voids (initial pores and cracks) V_v in the particle and the volume of cracks V_c are firstly quantified from the segmented volume images. Then V_c^* is calculated by subtracting the volume of initial pores from V_v . Thus the volume of initial pores penetrated by cracks $V_{p,c} = V_c - V_c^*$.

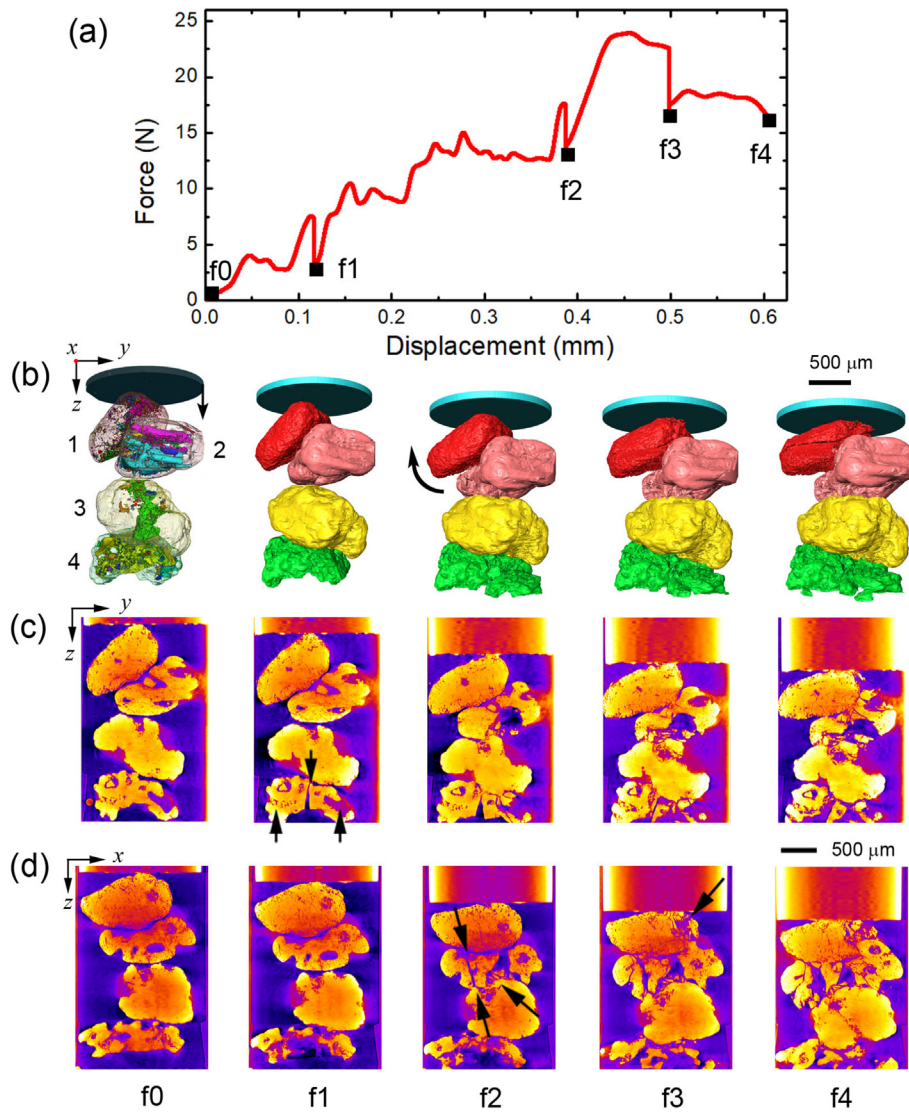


Fig. 6. Deformation and fracture of particles #1–#4. (a) Stress history. (b) 3D images, (c) y-z slices and (d) x-z slices of sand particles at selected instants (f0 – f4) marked by squares on the stress history.

Evolution of the crack porosity φ_c is presented in Fig. 9(b). φ_c increases considerably with increasing external loading, indicating that the cracks have traversed an increasing number of pores during propagation. The orientation and shape of the main crack which contains few

pores is determined by the stress state, while the branching cracks are prone to grow along initial pores, leading to a sharp increase of φ_c at later stages of particle breakage. Cracks do not always propagate straight in the direction perpendicular to the maximum tensile stress,

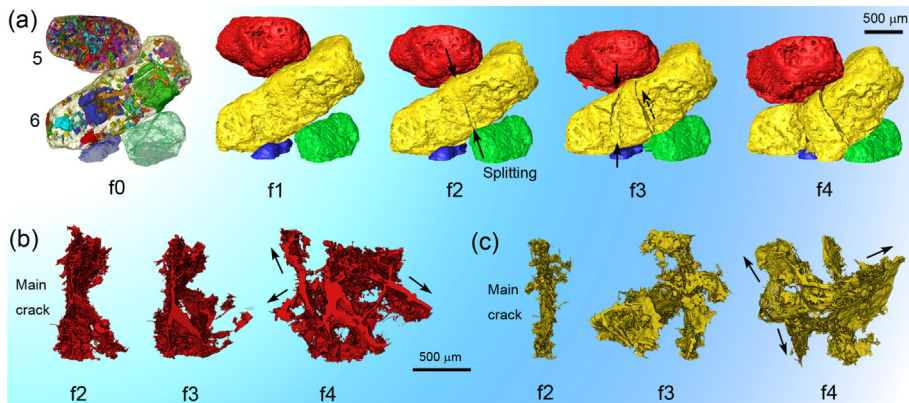


Fig. 7. 3D deformation and fracture of particles #5 and #6. (a) 3D images at selected instants (f0 – f4) marked by squares on the stress history (Fig. 6(a)), and evolution of 3D crack networks in particles (b) #5 and (c) #6.

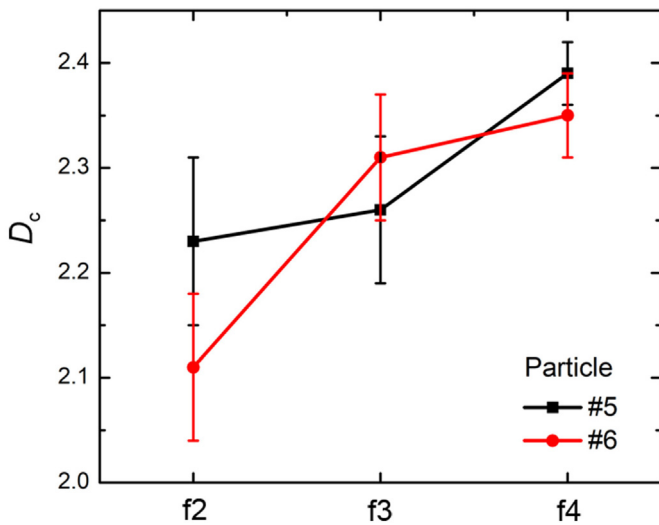


Fig. 8. Fractal dimension D_c of crack networks at different instants.

but are perturbed by local structural heterogeneities, e.g., pores. φ_c should therefore depend on the amount and spatial distribution of pores initially present in sand particles. φ_c of particle #5 is much higher than that of #6, probably because the dendritic and tubular pores in particle #5 (Fig. 7(a)) facilitate “cleavage” along pores. The cleavage breakage mode in carbonate sand particles is also applicable to other porous brittle materials, such as agglomerates and porous solids [12].

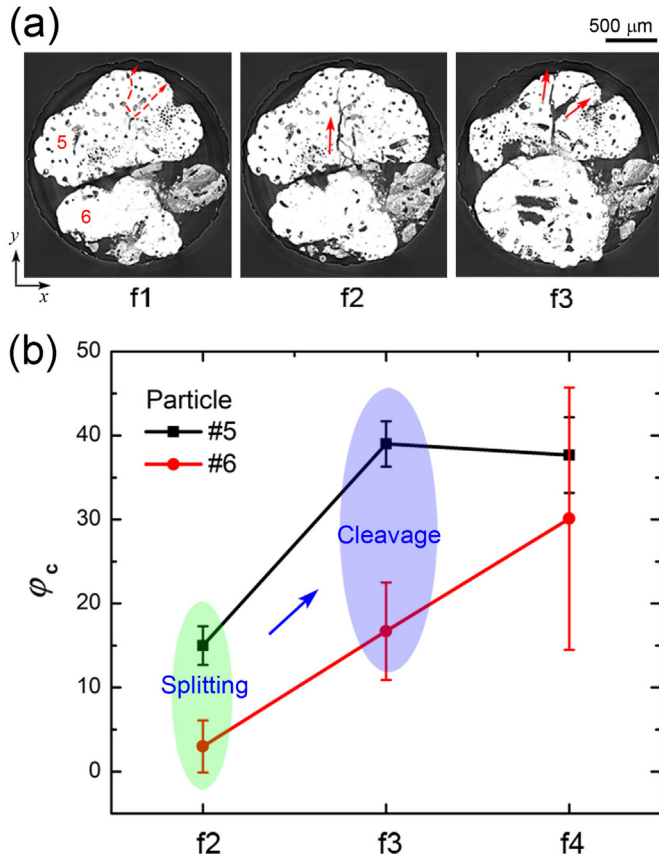


Fig. 9. (a) xy slices of particle #5 showing crack propagation along initial pores. (b) Fracture porosity φ_c at different instants.

3.4. Fragment morphology

It has been widely accepted that fragmentation is a scale-invariant process as manifested by fractal size distributions of fragments [9,56]. Using the 3D morphology of fragments, we now examine whether the fragmentation of carbonate sand particles is fractal. The fragments of particles #5 and #6 at a relatively stable state (while the fragment number does not increase significantly) are characterized, and the particle size distributions are plotted in Fig. 10(a) in double logarithmic coordinates. The intermediate stage of the distribution curve ($d_{fmin} < d_f < d_{fmax}$) is linear, i.e. fractal (marked by dashed lines). d_{fmin} and d_{fmax} are the lower and upper size limits for fractal distribution, respectively. The fractal dimension D_f is calculated as the inverse slope of linear stage, and is 1.77 ± 0.02 for particle #5 and 1.03 ± 0.01 for particle #6. The fractal dimension for particle #6 is considerably lower than that for particle #5, consistent with the lower fractal dimension of crack networks in particle #6 (Fig. 8). A more complex crack network is expected to result in a higher portion of fine fragments, and thus a higher fractal dimension for the fragment size distribution.

Particle #5 is taken as an example for characterization of the fragment morphology. The porosity of fragments n_1 is calculated and presented in Fig. 10(b). n_1 varies in a wide range (0–12%) with a mean of 1.3%, which is much smaller than the initial porosity of the mother particle (17.4%). In addition, the volume ratio of pores (n_2) that a fragment inherits from its mother particle is calculated for all fragments. n_2 is defined as the ratio between the volume of residual pores in fragments $V_{p,f}$ and the volume of initial pores in the particle $V_{p,0}$. It exhibits a power function with the fragment size (marked by the dashed line).

$$n_2 \propto d_f^{4.5}. \quad (9)$$

The cumulative volume ratio of pores in the fragments ($\sum n_2 = 47.4\%$) is much smaller than 100%, consistent with the fact that a considerable number of pores are in the crack networks (Fig. 9(b)).

The shape parameters of fragments for particle #5 are characterized and presented in Fig. 10(c) and (d). They vary considerably and do not show any well-defined size dependence. The classic sphericity index S_0 of fragments is linearly related to the convexity C_x (the dashed line, Fig. 10(c)), i.e.

$$S_0 = 1.0C_x - 0.18. \quad (10)$$

Similar linear relations were reported for silica sands [38]. However, this may not indicate that the sphericity of fragments is physically correlated to their angularity, since the S_1-C_x relationship (Fig. 10(c)) does not show any strong correlation. The reason is that S_0 contains information on both sphericity and surface roughness, and underestimates the fragment sphericity with low convexity. Fig. 10(d) shows that the fragment shape deviates far away from sphere, and the replacement of fragments with spheres as in previous DEM studies [27] is not appropriate for carbonate sands. The irregular shapes and porous structure of fragments should be considered for modelling particle breakage of carbonate sands.

To discuss the effects of surface roughness on the quantification of particle shape, two sphericity indices S_0 and S_1 along with the convexity C_x are compared between four artificial objects as presented in Fig. 11. A thorn ball (or ellipsoid) is composed of a smooth ball (or ellipsoid) and some spikes located on the surface according to the atom positions of C60. S_0 and S_1 yield the same sphericity value 1 for a smooth ball, but quite different sphericity values for a smooth ellipsoid. S_1 is more sensitive to deviation from sphere in shape. The spikes reduce considerably the convexity of the thorn ball and ellipsoid. S_0 yields lower sphericity values for the thorn ball and ellipsoid than those for the smooth ones, although they have a similar 3D shape. Therefore, S_0 is an integrated description of particle shape and surface roughness, and underestimates the sphericity of carbonate sand particles with rough surfaces. S_1

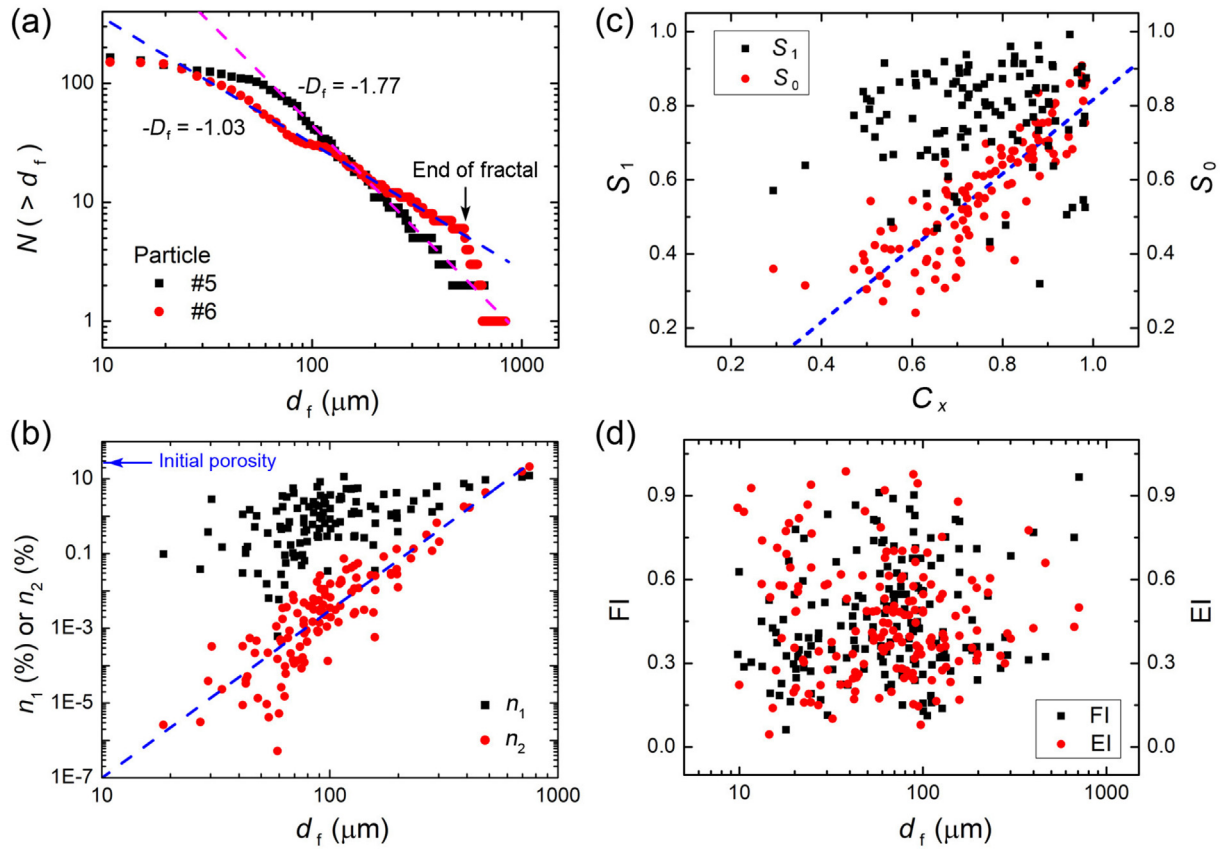


Fig. 10. 3D characterization of particle fragments. (a) Particle size distribution of fragments for particles #5 and #6. (b) Characterization of residual pores in the fragments of particle #5. n_1 : porosity of fragments; n_2 : ratio between the volume of residual pores in fragments and the volume of initial pores. The dashed line is a power-law fitting to the experimental data. (c) Shape parameters for fragments of particle #5. S_0 : classic sphericity index; S_1 : gyration-tensor defined sphericity index; EI: elongation index; FI: flatness index.

provides a more accurate description of the sphericity, and are not affected by the surface roughness.

4. Discussion

The fragment size distribution at the small size end ($<50 \mu\text{m}$) deviates away from the fractal distribution, probably owing to the undetected fine particles beyond the CT resolution limit. A calculation based on CT characterizations for particle #5 is carried out to examine whether fractal distribution is applicable to small fragments. Given N

$(>d_f) = C_0 d_f^{-D_f}$, the total volume of undetected particles V_{ud} is

$$V_{ud} = \frac{\pi C_0 D}{6(3-D)} (d_{fmin}^{3-D} - d_{bl}^{3-D}) - V_d, \tag{11}$$

where C_0 and D_f are 1.55×10^5 and 1.77 from the power law fitting (Fig. 10(a)); d_{fmin} is $54 \mu\text{m}$ for particle #5; d_{bl} is the breakage limit of calcium carbonate ($3 \mu\text{m}$) below which brittle-ductile transition prohibits breakage [57]; V_d is the detected volume of particles in the small-size range.

The ratio of the volume of undetected fragments to the volume of particle is calculated as 1.57% via Eq. (11), consistent with the result 1.65% quantified from direct CT measurements. Therefore, the fractal distribution can be extended to the breakage limit of calcium carbonate.

The fractal dimension for fragment size distribution of carbonate sand particles (1.0–1.8) is lower than that reported for silica sand particles (≥ 2.0) [38,58]. The probable reason is that crack propagation along the initial pores in carbonate sand particles results in fewer fine fragments than in silica particles from a statistical point of view. The fractal dimension for the fragment size distribution is much smaller than that for crack networks, since they are defined on different physical bases. However, they are positively correlated to each other. A more complex crack network leads to a higher portion of fine fragments, and thus a relatively higher fractal dimension for fragment size distribution.

The energy dissipation during particle breakage is achieved mainly via creating new fragment surfaces (surface energy), friction due to particle rearrangement and acoustic emission [8,59]. Accurate determination of the surface area of fragments is vital for understanding energy distributions during particle breakage. The surface area is significantly underestimated from the fragment size distribution with a spherical assumption [60], due to undetected micro fragments (Fig. 10(a)), high



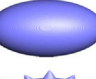
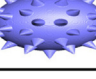
Object	S_0	S_1	C_x
	1	1	1
	0.73	1	0.54
	0.96	0.75	1
	0.70	0.75	0.54

Fig. 11. Artificial objects to examine the capacity of two sphericity indices.

angularity of fragments (Fig. 10(c) and (d)), and residual cracks embedded in fragments. The underestimation in surface area with spherical assumption can reach 50% for carbonate sands. The surface area of undetected fragments can be “recovered” with the fractal theory from the fragment surface area distribution [60], and accounts for about 6% of the total surface area in this study. Residual cracks have also been observed (via SEM or CT) in fragments of other brittle materials such as ceramics [61], silicon crystals [62], and glass particles [60]. Jiang et al. [60] reported that the surface area of undetected internal cracks in fragments of glass particles is comparable to the surface area of detected fragments. However, the internal cracks in our study accounts for only ~0.1% of the total crack surfaces. The probable reason is twofold. On the one hand, initial pores in carbonate sand particles facilitate crack coalescence and result in few residual cracks. On the other hand, the short loading pulse under high rate compression in Jiang et al. [60] leave more microcracks frozen in fragments. In addition, crack propagation along initial pores implies that not all crack surfaces are newly created by particle breakage (Fig. 9). This requires reconsideration of energy dissipation in modelling of particle breakage for carbonate sands.

5. Conclusions

With synchrotron-based in situ micro CT, the evolution of microstructures (morphology of particles, pores, cracks and their networks) of carbonate sands under mechanical loading are firstly identified and quantified. The fractal dimension of initial intraparticle pore networks increases with the porosity of sand particles following a power law. The in situ CT characterizations reveal clearly the structure–property relationship for carbonate sands, distinct from silica sands. The angular shape of carbonate sand particles facilitates bending fracture and results in a much lower fracture strength than that via tensile splitting. Particles with a lower sphericity and a higher porosity are more prone to break. 3D crack networks extracted from fractured particles imply considerable cleavage along initial pores. The crack network exhibits a fractal configuration and the fractal dimension increases with external loading. The resultant fragment size distributions also appear fractal and the fractal feature can be extended down to the breakage limit of calcium carbonate. Two sphericity indices are compared and examined with four artificial objects, and the sphericity index based on gyration-tensor analysis is more appropriate for shape description of carbonate sands. Crack propagation along the initial pores reduces the energy barrier for particle breakage and thus the fracture strength of particles. The results require careful consideration of 3D morphology of particle and pore networks in numerical modelling of carbonate sands.

Acknowledgements

This work was partially supported by the NSFC (No. 11802252, 11627901), National Key R&D Program of China (No. 2017YFB0702002), and the Scientific Challenge Project of China (No. TZ2018001). Use of the Advanced Photon Source was supported by the U.S. Department of Energy, Office of Science, Office of Basic Energy Sciences, under Contract No. DE-AC02-06CH11357.

Declarations of Competing Interest

None.

Appendix A. Appendix

A.1. Weibull statistics

A Weibull model has been widely used to analyze the scatter in apparent fracture strengths σ_s of sand particles (or granular

materials in general) directly obtained from the compression curves [18,63]. It assumes that σ_s and the probability of failure (P_f) follow a Weibull distribution,

$$P_f = 1 - \exp \left[- \left(\frac{\sigma_s}{\sigma_{s0}} \right)^m \right], \quad (\text{A.1})$$

where σ_{s0} is the characteristic fracture strength, and m is the Weibull modulus quantifying the extent of scatter in fracture strengths. The characteristic fracture strength and Weibull modulus can be obtained by linear fitting to the $P_f(\sigma_s)$ data with

$$\ln \ln \frac{1}{1-P_f} = m \ln \sigma_s + m \ln \frac{1}{\sigma_{s0}}. \quad (\text{A.2})$$

In experiments, P_f is commonly approximated as $\frac{i}{n+1}$, where n is the total number of tests, and i is the ranking of a test based on the strength data sorted in an ascending order. $\sigma_s = F/d^2$, where F is taken as the maximal force before a catastrophic force drop on the compression curve, and d is the equivalent diameter of a particle projection along the compression axis.

References

- [1] M. Randolph, S. Gourvenec, D. White, M. Cassidy, *Offshore Geotechnical Engineering*, Vol. 2, Spon Press, New York, 2011.
- [2] X.-Z. Wang, Y.-Y. Jiao, R. Wang, M.-J. Hu, Q.-S. Meng, F.-Y. Tan, Engineering characteristics of the calcareous sand in Nansha Islands, South China Sea, *Eng. Geol.* 120 (1–4) (2011) 40–47.
- [3] A. Wang, B. Lyu, Z. Zhang, K. Liu, H. Xu, D. Sun, The development of coral concretes and their upgrading technologies: a critical review, *Constr. Build. Mater.* 187 (2018) 1004–1019.
- [4] S.S. Sharma, M. Fahey, Degradation of stiffness of cemented calcareous soil in cyclic triaxial tests, *J. Geotech. Geoenviron. Eng.* 129 (7) (2003) 619–629.
- [5] M. Salem, H. Elmamlouk, S. Agaiby, Static and cyclic behavior of north coast calcareous sand in Egypt, *Soil Dyn. Earthq. Eng.* 55 (2013) 83–91.
- [6] D. Kong, J. Fonseca, Quantification of the morphology of shelly carbonate sands using 3D images, *Geotechnique* 68 (3) (2017) 249–261.
- [7] J. Huang, S. Xu, S. Hu, Effects of grain size and gradation on the dynamic responses of quartz sands, *Int. J. Impact Eng.* 59 (2013) 1–10.
- [8] J. Huang, S. Xu, S. Hu, Influence of particle breakage on the dynamic compression responses of brittle granular materials, *Mech. Mater.* 68 (2014) 15–28.
- [9] J.Y. Huang, S.S. Hu, S.L. Xu, S.N. Luo, Fractal crushing of granular materials under confined compression at different strain rates, *Int. J. Impact Eng.* 106 (2017) 259–265.
- [10] M.R. Coop, K.K. Sorensen, T. Bodas Freitas, G. Georgoutsos, Particle breakage during shearing of a carbonate sand, *Geotechnique* 54 (3) (2004) 157–163.
- [11] L. Ma, Z. Li, M. Wang, H. Wei, P. Fan, Effects of size and loading rate on the mechanical properties of single coral particles, *Powder Technol.* 342 (2019) 961–971.
- [12] H. Jiang, S. Xu, J. Shan, D. Wang, Y. Liu, L. Zhou, P. Wang, Dynamic breakage of porous hexagonal boron nitride ceramics subjected to impact loading, *Powder Technol.* 353 (2019) 359–371.
- [13] C.Q. Zhu, X.Z. Wang, R. Wang, H.Y. Chen, Q.S. Meng, Experimental microscopic study of inner pores of calcareous sand, *Mater. Res. Innov.* 18 (sup2) (2014) S2–207–S2–214.
- [14] E.T. Bowman, Particle shape characterisation using Fourier descriptor analysis, *Geotechnique* 51 (6) (2000) 545–554.
- [15] H. Liu, S. Kou, P.-A. Lindqvist, Numerical studies on the inter-particle breakage of a confined particle assembly in rock crushing, *Mech. Mater.* 37 (9) (2005) 935–954.
- [16] H. Mohammed, B. Briscoe, K. Pitt, The interrelationship between the compaction behaviour and the mechanical strength of pure pharmaceutical tablets, *Chem. Eng. Sci.* 60 (14) (2005) 3941–3947.
- [17] L. Tavares, Optimum routes for particle breakage by impact, *Powder Technol.* 142 (2) (2004) 81–91.
- [18] J. Huang, S. Xu, H. Yi, S. Hu, Size effect on the compression breakage strengths of glass particles, *Powder Technol.* 268 (2014) 86–94.
- [19] J. Shan, S. Xu, Y. Liu, L. Zhou, P. Wang, Dynamic breakage of glass sphere subjected to impact loading, *Powder Technol.* 330 (2018) 317–329.
- [20] F. Yu, Characteristics of particle breakage of sand in triaxial shear, *Powder Technol.* 320 (2017) 656–667.
- [21] Y. Xiao, H. Liu, Q. Chen, Q. Ma, Y. Xiang, Y. Zheng, Particle breakage and deformation of carbonate sands with wide range of densities during compression loading process, *Acta Geotech.* 12 (5) (2017) 1177–1184.
- [22] Y. Xiao, Z. Yuan, J. Chu, H. Liu, J. Huang, S. Luo, S. Wang, J. Lin, Particle breakage and energy dissipation of carbonate sands under quasi-static and dynamic compression, *Acta Geotech.* (2019) 1–15.
- [23] R.L. Michalowski, Z. Wang, S.S. Nadukuru, Maturing of contacts and ageing of silica sand, *Geotechnique* 68 (2) (2017) 133–145.
- [24] Y.P. Cheng, Y. Nakata, M.D. Bolton, Discrete element simulation of crushable soil, *Geotechnique* 53 (7) (2003) 633–641.

- [25] G. Ma, W. Zhou, R.A. Regueiro, Q. Wang, X. Chang, Modeling the fragmentation of rock grains using computed tomography and combined FDEM, *Powder Technol.* 308 (2017) 388–397.
- [26] B. Zhao, J. Wang, 3D quantitative shape analysis on form, roundness, and compactness with μ CT, *Powder Technol.* 291 (2016) 262–275.
- [27] O. Ben-Nun, I. Einav, The role of self-organization during confined comminution of granular materials, *Philos. Trans. R. Soc. Lond. A* 368 (1910) (2010) 231–247.
- [28] R. Hurley, S.A. Hall, J.E. Andrade, J. Wright, Quantifying interparticle forces and heterogeneity in 3D granular materials, *Phys. Rev. Lett.* 117 (9) (2016), 098005.
- [29] Z. Zheng, R. Ni, F. Wang, M. Dijkstra, Y. Wang, Y. Han, Structural signatures of dynamic heterogeneities in monolayers of colloidal ellipsoids, *Nat. Commun.* 5 (2014), 3829.
- [30] E. And'ò, S.A. Hall, G. Viggiani, J. Desrues, P. B'esuelle, Grain-scale experimental investigation of localised deformation in sand: a discrete particle tracking approach, *Acta Geotech.* 7 (1) (2012) 1–13.
- [31] J.Y. Huang, L. Lu, D. Fan, T. Sun, K. Fezzaa, S.L. Xu, M.H. Zhu, S.N. Luo, Heterogeneity in deformation of granular ceramics under dynamic loading, *Scr. Mater.* 111 (2016) 114–118.
- [32] G. Davis, J. Elliott, Artefacts in X-ray microtomography of materials, *Mater. Sci. Technol.* 22 (9) (2006) 1011–1018.
- [33] F. Fusseis, X. Xiao, C. Schrank, F.D. Carlo, A brief guide to synchrotron radiation-based microtomography in (structural) geology and rock mechanics, *J. Struct. Geol.* 65 (3) (2014) 1–16.
- [34] A. Hasan, K.A. Alshibli, Experimental assessment of 3D particle-toparticle interaction within sheared sand using synchrotron microtomography, *Geotechnique* 60 (5) (2015) 369–379.
- [35] J. Fonseca, S. Nadimi, C.C. Reyes-Aldasoro, C. OSullivan, M.R. Coop, Image-based investigation into the primary fabric of stress-transmitting particles in sand, *Soils Found.* 56 (5) (2016) 818–834.
- [36] M. Wiebicke, E. And'ò, I. Herle, G. Viggiani, On the metrology of interparticle contacts in sand from x-ray tomography images, *Meas. Sci. Technol.* 28 (12) (2017) 124007.
- [37] T. Afshar, M.M. Disfani, G.A. Narsilio, A. Arulrajah, Post-breakage changes in particle properties using synchrotron tomography, *Powder Technol.* 325 (2018), 530–544.
- [38] B. Zhao, J. Wang, M.R. Coop, G. Viggiani, M. Jiang, An investigation of single sand particle fracture using X-ray micro-tomography, *Geotechnique* 65 (8) (2015) 625–641.
- [39] B. Zhou, J. Wang, H. Wang, Three-dimensional sphericity, roundness and fractal dimension of sand particles, *Geotechnique* 68 (1) (2017) 18–30.
- [40] M. Wu, J. Wang, Reassembling fractured sand particles using fracture-region matching algorithm, *Powder Technol.* 338 (2018) 55–66.
- [41] B.X. Bie, J.Y. Huang, D. Fan, T. Sun, K. Fezzaa, X.H. Xiao, M.L. Qi, S.N. Luo, Orientation-dependent tensile deformation and damage of a T700 carbon fiber/epoxy composite: a synchrotron-based study, *Carbon* 121 (2017) 127–133.
- [42] D. Grsoy, C.F. De, X. Xiao, C. Jacobsen, Tomopy: a framework for the analysis of synchrotron tomographic data, *J. Synchrotron Radiat.* 21 (Pt 5) (2014) 1188–1193.
- [43] G. Kerckhofs, J. Schrooten, T. Van Cleynenbreugel, S.V. Lomov, M. Wevers, Validation of x-ray microfocus computed tomography as an imaging tool for porous structures, *Rev. Sci. Instrum.* 79 (1) (2008), 013711.
- [44] S. Weis, M. Schroter, Analyzing X-ray tomographies of granular packings, *Rev. Sci. Instrum.* 88 (5) (2017) 051809.
- [45] F. Meyer, S. Beucher, Morphological segmentation, *J. Vis. Commun. Image R.* 1 (1) (1990) 21–46.
- [46] L. Vincent, P. Soille, Watersheds in digital spaces: an efficient algorithm based on immersion simulations, *IEEE T. Pattern Anal.* (6) (1991) 583–598.
- [47] D.S. Bright, E.B. Steel, Two-dimensional top hat filter for extracting spots and spheres from digital images, *J. Microsc.* 146 (2) (1987) 191–200.
- [48] J. Bontaz-Carion, Y.-P. Pellegrini, X-ray microtomography analysis of dynamic damage in tantalum, *Adv. Eng. Mater.* 8 (6) (2006) 480–486.
- [49] Y. Yao, H.W. Chai, C. Li, B.X. Bie, X.H. Xiao, J.Y. Huang, M.L. Qi, S.N. Luo, Deformation and damage of sintered low-porosity aluminum under planar impact: microstructures and mechanisms, *J. Mater. Sci.* 53 (6) (2018) 4582–4597.
- [50] Q. Wang, Z. Liang, X. Wang, W. Zhao, Y. Wu, T. Zhou, Fractal analysis of surface topography in ground monocrystal sapphire, *Appl. Surf. Sci.* 327 (2015) 182–189.
- [51] Y. Xiao, Z. Yuan, Y. Lv, L. Wang, H. Liu, Fractal crushing of carbonate and quartz sands along the specimen height under impact loading, *Constr. Build. Mater.* 182 (2018) 188–199.
- [52] K. Foroutan-Pour, P. Dutilleul, D.L. Smith, Advances in the implementation of the box-counting method of fractal dimension estimation, *Appl. Math. Comput.* 105 (23) (1999) 195–210.
- [53] G. McDowell, A. Amon, The application of Weibull statistics to the fracture of soil particles, *Soils Found.* 40 (5) (2000) 133–141.
- [54] J.-m. Zhang, M.-d. Duan, D.-l. Wang, Y. Zhang, Particle strength of calcareous sand in nansha islands, South China Sea, *Adv. Civ. Eng. Mater.* 8 (1) (2019) 355–364.
- [55] F. Renard, D. Bernard, J. Desrues, A. Ougier-Simonin, 3D imaging of fracture propagation using synchrotron X-ray microtomography, *Earth Planet. Sci. Lett.* 286 (1–2) (2009) 285–291.
- [56] D. Turcotte, Fractals and fragmentation, *J. Geophys. Res. Sol. Ea.* 91 (B2) (1986) 1921–1926.
- [57] K. Kendall, The impossibility of comminuting small particles by compression, *Nature* 272 (5655) (1978) 710.
- [58] Y. Nakata, Y. Kato, M. Hyodo, A.F. Hyde, H. Murata, One-dimensional compression behaviour of uniformly graded sand related to single particle crushing strength, *Soils Found.* 41 (2) (2001) 39–51.
- [59] P. Wang, C. Arson, Energy distribution during the quasi-static confined comminution of granular materials, *Acta Geotech.* 13 (5) (2018) 1075–1083.
- [60] S. Jiang, L. Shen, F. Guillard, I. Einav, Energy dissipation from two-glassbead chains under impact, *Int. J. Impact Eng.* 114 (2018) 160–168.
- [61] C.J. Shih, M.A. Meyers, V.F. Nesterenko, S.J. Chen, Damage evolution in dynamic deformation of silicon carbide, *Acta Mater.* 48 (9) (2000) 2399–2420.
- [62] J.Y. Huang, J.W. Huang, T. Sun, K. Fezzaa, S.L. Xu, S.N. Luo, Dynamic deformation and fracture of single crystal silicon: fracture modes, damage laws, and anisotropy, *Acta Mater.* 114 (2016) 136–145.
- [63] K. Trustrum, A.D.S. Jayatilaka, On estimating the Weibull modulus for a brittle material, *J. Mater. Sci.* 14 (5) (1979) 1080–1084.